Geophysical Research Letters

RESEARCH LETTER
10.1029/2020GL091527

Auroral Energy Flux and Joule Heating Derived From Global Maps of Field-Aligned Currents

R. M. Robinson[1] and **L. J. Zanetti**[2]

[1]The Catholic University of America, Washington, DC, USA, [2]National Oceanic and Atmospheric Administration, Laurel, MD, USA

Key Points:

- We calculate hemispherically integrated precipitating particle energy fluxes and Joule heating from global maps of field-aligned currents
- Energy input from Joule heating and precipitating particles correlates well with increases in the Sym-H index occurring about 1 h later
- Joule heating in the ionosphere during substorm growth phase is approximately equal to magnetic energy released during substorm expansion

Supporting Information:

Supporting Information may be found in the online version of this article.

Correspondence to:

R. M. Robinson,
bobr@inspacenow.com

Citation:

Robinson, R. M., & Zanetti, L. J. (2021). Auroral energy flux and Joule heating derived from global maps of field-aligned currents. *Geophysical Research Letters*, *48*, e2020GL091527. https://doi.org/10.1029/2020GL091527

Received 1 NOV 2020
Accepted 25 JAN 2021

Abstract We calculate auroral energy flux and Joule heating in the high-latitude ionosphere for 27 geomagnetically active days using two-dimensional maps of field-aligned currents determined by the Active Magnetosphere and Planetary Response Experiment. The energy input to the ionosphere due to Joule heating increases more rapidly with geomagnetic activity than that due to precipitating particles. The energy flux varies more smoothly with time than Joule heating, which is impulsive in nature on time scales from minutes to tens of minutes. These impulsive events correlate well with recoveries in the Sym-H index, with the maximum correlation when compared to Sym-H recoveries 70 min later. Because of prior studies that have associated transient recoveries of Sym-H with substorm expansions, the delay found here suggests that dissipation of energy in the ionosphere occurs during the substorm growth phase prior to the release of magnetic energy caused by diversion of tail currents.

Plain Language Summary Storms on the sun release radiation and energetic particles that travel through space and impact Earth. Energy from this impact is temporarily stored in the magnetic bubble formed by Earth's magnetosphere, dissipating gradually over time. At high-latitudes, energy is lost from the magnetosphere by the precipitation of energetic particles into the atmosphere, and by the frictional heating associated with electric currents in Earth's ionosphere. We model the high-latitude energy input to Earth's atmosphere from these two sources using 27 days of data from the 66 satellites of the Iridium constellation. We find that the energy input from particle impact is smoothly varying with time, in contrast to the frictional energy loss from the electric currents, which is impulsive in nature, characterized by enhancements that last several to several tens of minutes. These short-lived energy loss events occur about an hour before changes in a magnetic index that measures the energy content of Earth's magnetosphere. The frictional heating occurs in conjunction with magnetic energy storage in the magnetosphere. The subsequent release of this magnetic energy causes the change in the magnetic index.

1. Introduction

At high-latitudes, energy is deposited in Earth's upper atmosphere and ionosphere through solar extreme ultraviolet (EUV) radiation, auroral particle precipitation, Joule heating from electric currents, and gravity wave propagation from the lower atmosphere. During geomagnetically quiet times, forcing from the lower atmosphere is important, while during geomagnetic storms, auroral particle precipitation and Joule heating dominate.

Although energy input from solar EUV is well-understood, global specification of energy input from auroral precipitation and Joule heating remains difficult. For energy flux from precipitation, empirical models such as OVATION PRIME (Newell et al., 2009, 2014) have been used. The energy input from Joule heating relies on auroral electrodynamic models, such as the Assimilative Model of Ionospheric Electrodynamics (AMIE; Crowley & Hackert, 2001; Lu et al., 1996; Richmond, 1992), which routinely takes in available observations from magnetometers, radars, and optical sensors to construct maps of ionospheric electric fields, currents, and Joule heating. Weimer (1995) and (2005) constructed solar wind-driven empirical models of electric potentials and Joule heating based on electric field and field-aligned current data from the Dynamics Explorer-2 satellite. Other models determine auroral parameters by simulating the magnetosphere-ionosphere response to solar wind forcing, such as the Thermosphere Ionosphere Mesosphere Electrodynamics General Circulation Model (Roble & Emery, 1983; Roble & Ridley, 1987; Qian et al., 2014), the Global Ionosphere Thermosphere Model (GITM; Ridley et al., 2006), and the Grand Unified Magnetosphere-Ionosphere

Coupling Simulation model (GUMICS; Janhunen et al., 2012). Cousins et al. (2015) derived auroral electrodynamic parameters by combining SuperDARN data with measurements of field-aligned currents from the Active Magnetosphere and Planetary Response Experiment (AMPERE).

Here we build on three recent studies that use global maps of field-aligned currents from AMPERE to determine auroral conductances, energy fluxes, electric fields, currents, and Joule heating. Robinson et al. (2018) used AMPERE data with far ultraviolet measurements from the Global Ultraviolet Imager on the Thermosphere Ionosphere Mesosphere Energetics and Dynamics satellite to derive statistical relations between auroral energy flux and field-aligned currents. Robinson, Kaeppler, et al. (2020) used a similar methodology to derive statistical relations between field-aligned currents and auroral conductances based on AMPERE and Poker Flat Incoherent Scatter Radar observations, respectively. Robinson, Zanetti, et al. (2020) combined the results from both these studies to fully specify high-latitude auroral electrodynamic parameters. They showed that the ionospheric currents derived by this method reproduced the SuperMAG SME index (Gjerloev 2009, 2012) with a correlation coefficient of 0.84.

In this study, we focus on the determination of energy input from both particle precipitation and Joule heating based on AMPERE field-aligned current maps using the results of the Robinson et al. (2018) and Robinson, Kaeppler, et al. (2020) studies. Although these methods produce two-dimensional maps of energy flux and Joule heating, we confine the present study to the hemispherically integrated quantities from both hemispheres. We begin by showing examples of the calculation of global energy flux and Joule heating. We then show how these are related to the cross polar cap potential and the auroral electrojet (AE) index, also derived from AMPERE field-aligned current maps, for 27 geomagnetically active days. We show that global energy input rates are correlated with positive excursions of the Sym-H magnetic index, consistent with previous studies relating recovery of Dst and Sym-H to changes in tail currents caused by substorm injections (e.g., Iyemori & Rao, 1996; Ohtani et al., 2001). We discuss the implications of these results to energy transfer associated with magnetospheric storms and substorms.

2. Determination of Auroral Electrodynamic Parameters from AMPERE

AMPERE makes use of magnetometer data from the Iridium satellite constellation (Anderson et al., 2000, 2014). The transverse magnetic perturbations are analyzed to generate maps of field-aligned currents poleward of 40° magnetic latitude in both the northern and southern hemispheres with a uniform grid spacing of 1° in magnetic latitude and 1 hour in magnetic local time. Maps are currently available every 2 min from January 2010 to September 2017. Table S1 lists the 27 geomagnetically active days used for the current study.

Given the two-dimensional distribution of field-aligned currents and conductances, electric fields can be calculated from current continuity,

$$J_{\parallel} = \nabla \cdot J_{\perp} = \nabla\left(\overline{\overline{\Sigma}}\,\overline{E}\right) \tag{1}$$

where $J_{\parallel}$ is the current density along the magnetic field, assumed vertical in the high-latitude ionosphere, $\overline{E}$ is the electric field, $\overline{\overline{\Sigma}}$ is the conductivity tensor, and $\overline{J}_{\perp}$ is given by

$$\overline{J}_{\perp} = \sum_P \overline{E} - \sum_H \left(\overline{E} \times \overline{B}\right) / \left|B\right| \tag{2}$$

The global distribution of Pedersen and Hall conductance, $\sum_P$ and $\sum_H$, is determined here using the results of Robinson, Kaeppler, et al. (2020). With the field-aligned currents and conductances known, the electric potential is calculated by numerical solution of a second-order differential equation (Robinson, Zanetti, et al., 2020). The electric fields are then used with the conductances to calculate the horizontal currents and Joule heating. Robinson, Zanetti, et al. (2020) showed that the currents derived by this method for 30 geomagnetically active days reproduce the SuperMAG magnetic indices with a correlation coefficient of 0.84. In addition to the electrodynamic parameters, the energy input from precipitating particles can be similarly determined from the field-aligned current maps, making use of the results of the study by Robinson et al. (2018) relating field-aligned currents to precipitating particle energy flux. Thus, the spatial

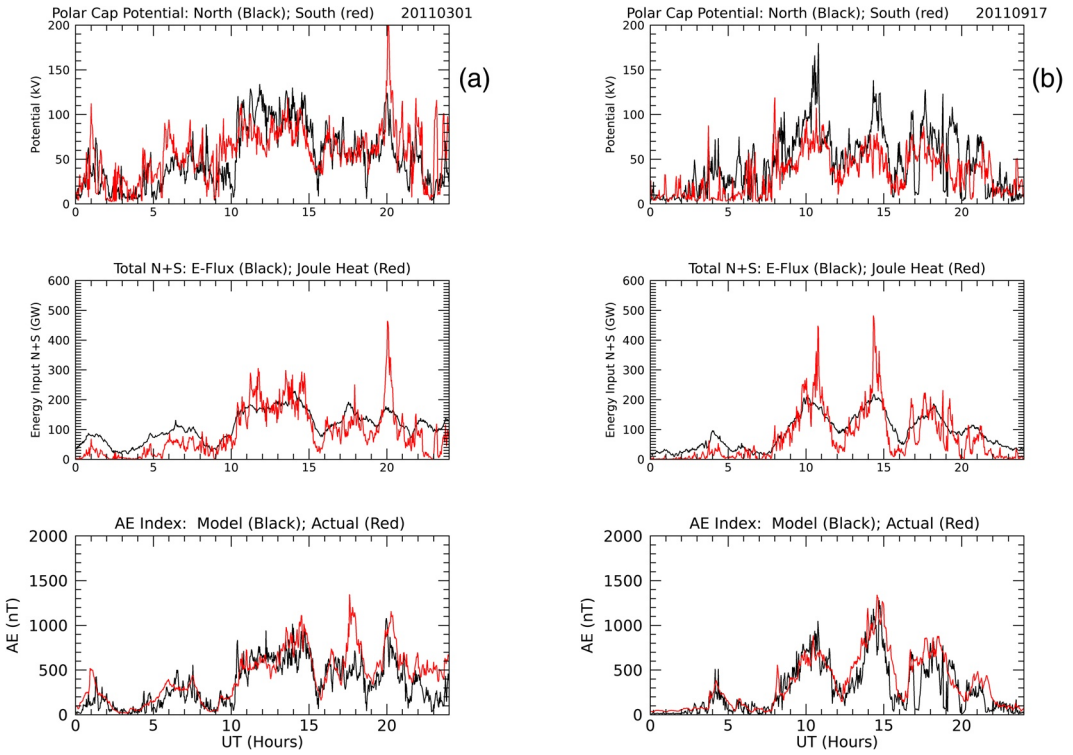

Figure 1. Auroral precipitation and electrodynamic parameters for two geomagnetically active days: (a) March 1, 2011 and (b) September 17, 2011. The top panel is the cross polar cap potential in the northern hemisphere and southern hemisphere, the middle panel is the total hemispherically integrated precipitating particle energy flux and Joule heating, combining the northern and southern hemispheres, and the bottom panel is the actual and modeled AE index.

distribution, strength, and direction of field-aligned currents contain information that allows for the determination of both energy flux from precipitating particles and Joule heating. AMPERE maps represent 10 min of data updated every 2 min.

Although the methods described above yield two-dimensional maps of conductances, electric field, horizontal current, and Joule heating, in the present study we show only the one-dimensional forms of the parameters: cross polar cap potential, the AE index, and the hemispherically integrated precipitating particle energy flux and Joule heating. The hemispherically integrated quantities are determined by computing the surface integrals from 40° to 90° magnetic latitude. The cross polar cap potential is determined from the maximum and minimum values of the potential distribution in each hemisphere. The AE index is derived by calculating magnetic perturbations at the 12 northern hemisphere AE magnetometer stations using the same method described in Robinson, Zanetti, et al. (2020). All one-dimensional quantities are calculated at two-min intervals. Because of the spatial resolution of the field-aligned current measurements and the subsequent AMPERE fitting procedure, our results capture electrodynamic parameters associated with auroral features on scales larger than tens of kilometers. Our results assume smaller scale features do not contribute significantly to the global quantities studied here.

Examples of the results of these calculations are shown in Figure 1 for two of the geomagnetically active days used for this study. The top panels show the polar cap potential in the northern and southern hemispheres, the middle panels show the combined hemispherically integrated precipitating particle energy flux and Joule heat from the northern and southern hemispheres. The bottom panels show the modeled and actual values of the AE index. The good agreement between the two is an indicator of the accuracy of the derived electric fields and currents. Errors in the derived parameters are discussed further below.

3. Relations Between Global Auroral Parameters

An advantage of the approach described above is that it can be applied routinely to the entire AMPERE data base, which currently extends from January 2010 to September 2017. The ability to analyze multiple data sets allows examination of how the global auroral parameters are statistically related. As an example, Figure 2 shows plots of the relationship between the various parameters for the 27 days used for this study. With quantities calculated every 2 min, each panel includes more than 16,000 data points.

Figures 2a and 2b show that the energy flux remains below 200 GW, while the energy input from Joule heat can exceed 400 GW during active times. The two sources of energy input are compared directly in Figure 2e. Figure 2f relates the AE index to the polar cap potential. The distribution of points agrees with the results of Weimer et al. (1990) based on Dynamics Explorer satellite observations, shown by the red curve in the figure.

4. Correlation Between Joule Heating and Changes in Sym-H

The hemispherically integrated energy flux and Joule heating represent a significant source of energy dissipation to the ionosphere. To examine the relation between this energy loss from the magnetosphere and the corresponding energy changes in the ring current, we correlated the total ionospheric energy dissipation with variations in the Sym-H magnetic index. Examples are shown in Figure 3 for four geomagnetically active days. The top panels show the Sym-H index. The 1-min Sym-H values were averaged over 10-min intervals every 2 min to match the AMPERE sampling rate. The middle panels show the change in Sym-H over 2 min for only those intervals with positive changes. The bottom panels show the hemispherically integrated energy flux and Joule heating, combining northern and southern hemisphere values. The vertical blue bars indicate those intervals where the change in Sym-H is positive over intervals greater than DT = 20 min. The time axes in the bottom panels have been shifted 1 hour later. This was done to bring some of the peaks in the Joule heating rate into the blue-shaded regions marking the positive slope periods in the Sym-H index. Similar plots for all 27 days used in this study are shown in Figure S1 for DT = 20 min and a time shift of 60 min.

Examination of Figures 3 and S1 shows that the times of net increases in Sym-H over 20 min often correlate well with localized peaks in the Joule heating rate. The energy flux from precipitation during these intervals is also enhanced, but in general the increases in energy flux are less prominent than the associated Joule heating enhancements. We use the Dessler-Parker-Sckopke (DPS) relationship (Dessler & Parker, 1959; Liemohn, 2003) to relate the change in Sym-H to a corresponding change in ring current energy content:

$$\Delta\text{Sym - H}\left[nT\right] = -2.8 \times 10^{13}\ \text{Joules} \tag{3}$$

The negative sign here indicates that when Sym-H increases, ring current energy decreases. Using this formula, we calculate the decrease in ring current energy corresponding to the increase in Sym-H from the beginning to the end of the blue-shaded time intervals. By integrating the Joule heating and energy flux over the same time interval, we can relate the ionospheric energy dissipation by Joule heating and energy flux to the change in ring current energy as indicated by the change in Sym-H.

Figure 4 shows the correlations between the global energy input (Joule heating plus particle precipitation) and the loss in ring current energy as indicated by the increase in the Sym-H index over the same time intervals for three values of DT and a time shift of 70 min. The legend in each panel of Figure 4 gives the value of DT, the time shift, the number of intervals found over 27 days, and the correlation coefficient between the energy loss in the ionosphere and the energy loss from the ring current as indicated by the change in Sym-H. The red lines indicate exact agreement between the two loss rates. Log scales are used for both axes to capture the full dynamic range of the quantities. Although we shifted the times of the energy input values for the example days shown in Figure 3 by 1 h, this shift did not yield the best overall agreement when applied to all 27 days. The parameters shown in Figure 4 yielded the best correlation coefficients between the two data sets, although the difference between time shifts from 0 to 90 min was less than 20%.

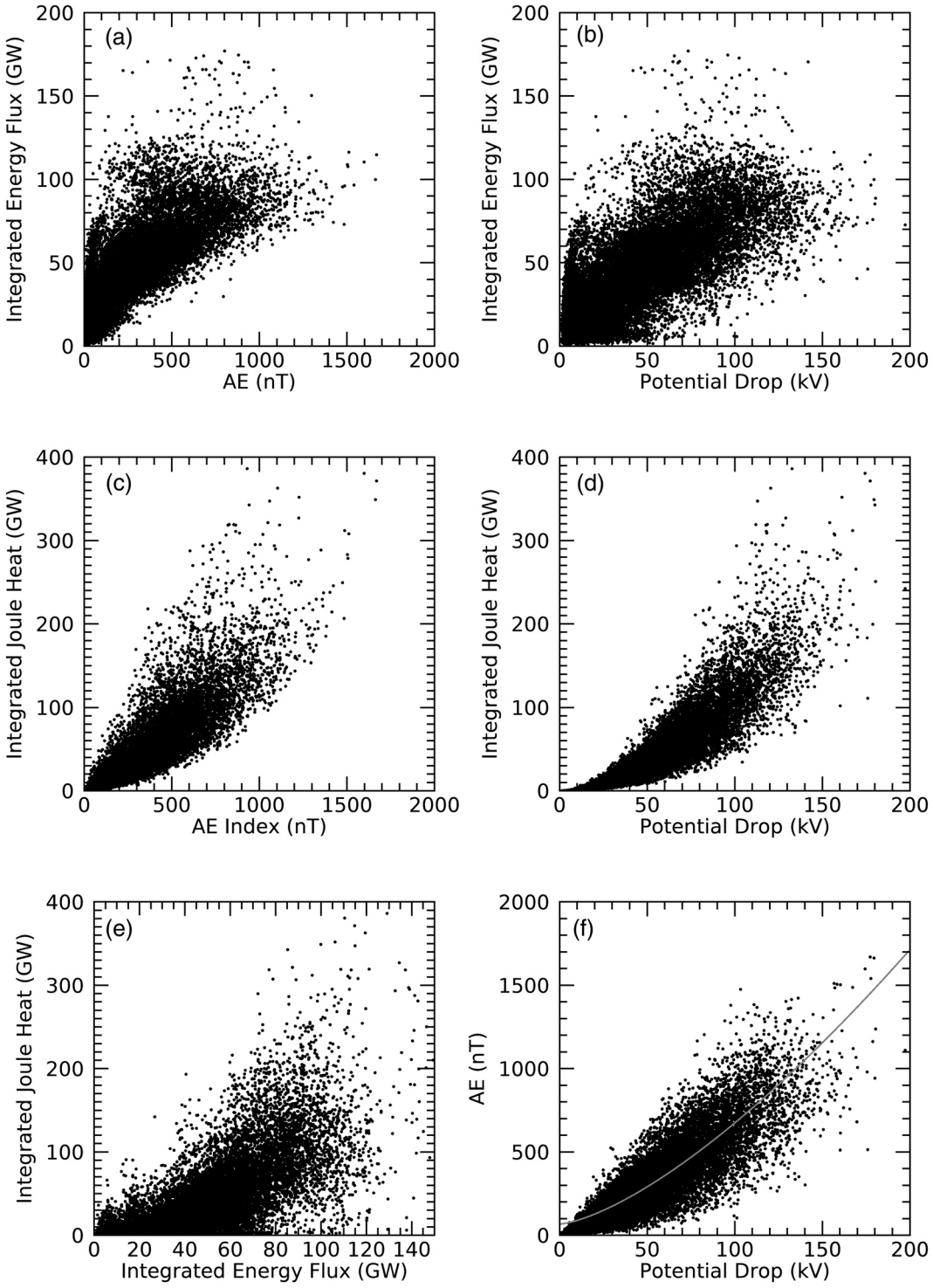

Figure 2. Scatter plots of global auroral parameters for 27 geomagnetically active days. All parameters are derived from AMPERE field-aligned current maps derived every 2 min. The red curve in Figure 2f is the relation between AE and polar cap potential found by Weimer et al. (1990). AMPERE, Active Magnetosphere and Planetary Response Experiment.

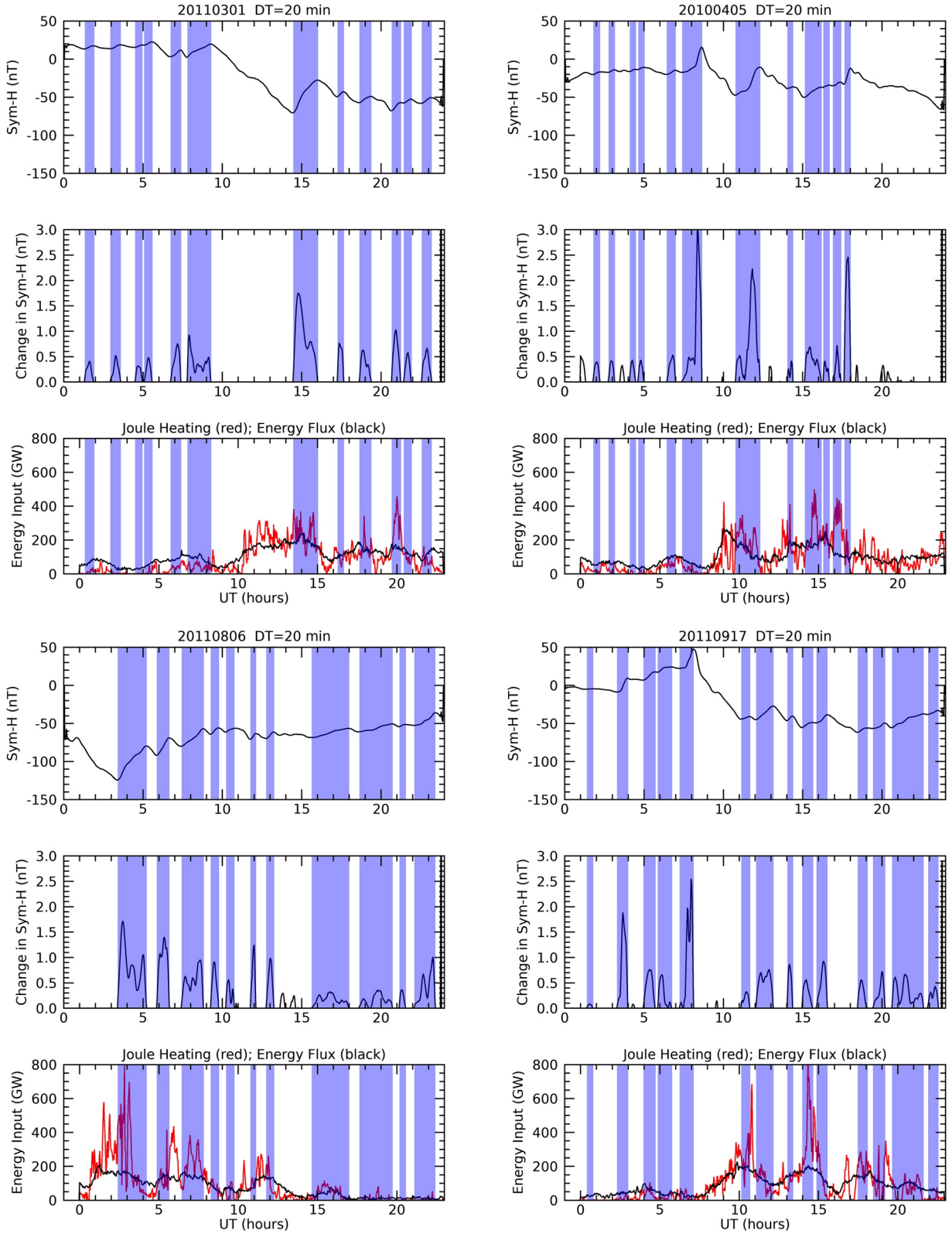
20110301 DT=20 min
20100405 DT=20 min
Sym-H (nT)
Change in Sym-H (nT)
Joule Heating (red); Energy Flux (black)
Energy Input (GW)
UT (hours)
20110806 DT=20 min
20110917 DT=20 min

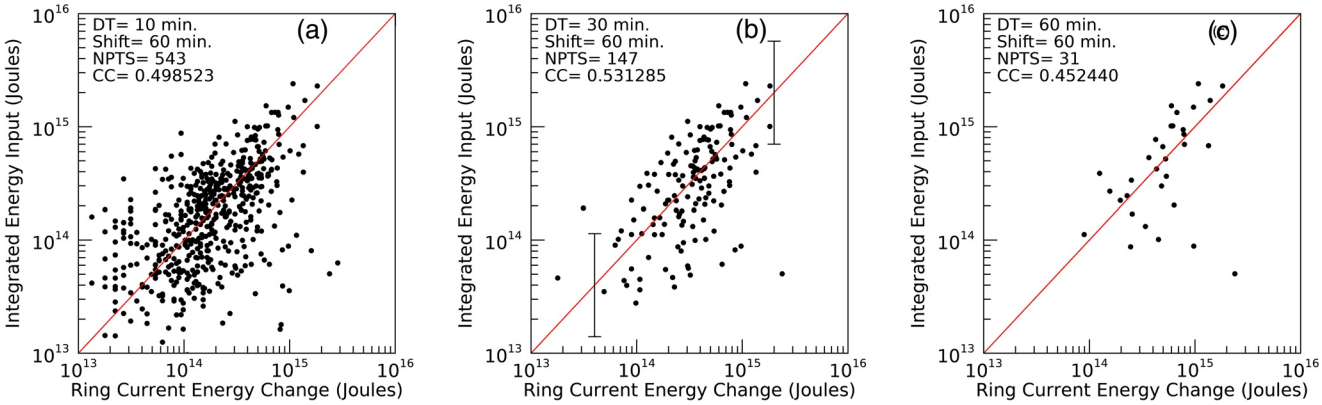

Figure 4. Correlation between hemispherically integrated Joule heating plus precipitating particle energy flux over the intervals of positive slope in Sym-H and ring current energy loss as determined from Equation 3. The error bars in the center panel show the approximate errors in the energy input determinations.

The error bars in the center panel of Figure 4 represent an estimate of the uncertainties in the energy input determination. From Robinson, Zanetti, et al. (2020), the average fractional difference between actual and simulated AE index is 0.3. We use this as the uncertainty in the horizontal current J. From Robinson, Kaeppler, et al. (2020), the average fractional error in Pedersen conductance determined from field-aligned currents is 0.6. With Joule heat given by $J^2 / \sum_P$, then the fractional error is 0.7. From Robinson et al. (2018), the uncertainty in the specification of energy flux from field-aligned current is about 20%, which results in an overall uncertainty in localized energy input of about 78% percent. The error bars in Figure 4 span a factor of 8 in the energy input values to reflect this uncertainty.

A source of systematic error in the global measurements is the limited spatial resolution of the AMPERE data, which results in the neglect of contributions from small-scale auroral features, such as discrete arcs. Newell et al. (2009) found the average hemispheric energy input due to particle precipitation in monoenergetic aurora is about 6 GW during active conditions. This is small relative to the global energy input values found here except during the quietest time intervals.

5. Discussion

We calculated auroral electrodynamic parameters along with hemispherically integrated precipitating particle fluxes and Joule heating derived from AMPERE maps of field-aligned currents. The energy input to the ionosphere due to Joule heating increases more rapidly with geomagnetic activity than that due to precipitating particles. Also, the temporal variation of the energy flux during geomagnetically active periods is relatively smooth compared to the changes in the Joule heating, which are impulsive in nature on time scales from minutes to tens of minutes. Very often, the spike-like increases in global Joule heating correlate with intervals of positive slopes in the Sym-H magnetic index. We used the DPS relation (Dessler & Parker, 1959) to determine the ring current energy change associated with these positive excursions. We varied both the time over which the positive excursions last and the time shift between the Joule heating and Sym-H time series. The correlation coefficients maximize for a shift of 70 min between the Joule heating and the ring current energy as indicated by the change in Sym-H. For this time shift, the correlation coefficients varied from 0.46 to 0.54 for discrete events lasting from 10 to 60 min. Many of the largest increases in Sym-H are associated with sudden storm commencements (SSCs). Our results show little enhancement in the global

Figure 3. Stackplots showing the relationship between Sym-H and the hemispherically integrated Joule heating and precipitating particle energy flux for four days. The top panels show the Sym-H index, where the 1-minute values were averaged over 10-min intervals every 2 min to match the AMPERE sampling rate. The middle panels show the change in Sym-H over each two-min interval for positive changes only. The bottom panel shows the total energy input from precipitating particles and Joule heating combining northern and southern hemisphere values. Note the one-hour offset in the UT axis for the lower panels in each set of three. The vertical blue bars indicate those intervals where the change in Sym-H is positive over intervals greater than DT = 20 min. AMPERE, Active Magnetosphere and Planetary Response Experiment.

rates of energy dissipation from precipitation and Joule heating at these times either because they are weak or highly localized. These associated data points appear in the lower right in the three panels of Figure 4. If we eliminate the times of SSCs from the data, the correlation coefficients between energy dissipation and ring current energy change are 0.68, 0.62, and 0.71 for the three values of DT shown.

The intervals of positive excursion in the Sym-H index shown in Figures 3 and S1 are sporadic in nature, and occur throughout all storm phases. The change in Sym-H over these intervals, when converted to energy according to the DPS relation, correlates with global ionospheric energy dissipation integrated over the same time interval. The correlation coefficients increase by 15% from a time shift of 0 min to a maximum of 70 min between the two quantities. With a 70-min time shift, many of the impulsive increases in the global Joule heating rate coincide with isolated positive excursions in Sym-H, while in other cases the positive excursions occur within an extended interval of enhanced energy dissipation. In either case, the magnitude of the energy dissipation rate integrated over the interval correlates well with the equivalent energy loss rate from the ring current as indicated by the change in Sym-H.

Iyemori and Rao (1996) associated positive excursions in Sym-H during geomagnetic storms with the expansion phase of substorms (the time of dipolarization of magnetotail field lines). This result contradicted the conventional view that dipolarization of the tail magnetic field injects energetic particles into the inner magnetosphere, strengthening the ring current and resulting in a decrease in Dst (larger – Dst). Siscoe and Petschek (1997) accounted for this in terms of the partitioning of energy released between thermal energy and magnetic energy during the substorm expansion phase. If more magnetic energy is dissipated by Joule heating in the ionosphere than is supplied in energizing particles during dipolarization, then Dst will increase (weakening ring current).

Ohtani et al. (2001) performed a superposed epoch analysis of 59 storms to show that the start of recovery in Dst (or Sym-H) coincides with dipolarization events as determined from magnetic field observations at geosynchronous orbit. They attributed this increase in Dst to the diversion of the cross-tail current, which contributes approximately 20% to the surface magnetic disturbances that make up the Dst index.

The discrete excursions of Sym-H studied here have time scales as short as 10 min, and often correlate with Joule heating enhancements of similar duration. To the extent that these events are substorms of varying durations and strengths, the delay of 70 min between the discrete Joule heating intervals and the subsequent positive excursions in Sym-H is inconsistent with the explanation given by Siscoe and Petschek (1997), in which the energy dissipation from Joule heating occurs at the same time as dipolarization. The study by Ohtani et al. (2001) focuses on the effects of diversion of tail currents at the same time as the minimum in Dst, suggesting that substorm expansion phases mark the recovery of the Dst index, but not necessarily the start of the storm recovery.

Interestingly, the superposed epoch analysis performed by Ohtani et al. (2001) showed that on average the southward interplanetary magnetic field that initiates the geomagnetic storm turns northward 70 min before the time of minimum Dst. The similarity between this time delay and the one found here suggests that the northward turning might also mark the start of energy dissipation in the ionosphere due to Joule heating. This may also coincide with the beginning of the substorm growth phase. That the energy released in the subsequent substorm dipolarization is approximately equal to the ionospheric energy input rate integrated over the same time interval 70 min earlier suggests that during the substorm growth phase equal amounts of solar wind energy go into stored magnetic energy in the tail and ionospheric energy dissipation. Note that because of the large uncertainties in our measurements of energy input, we can only say that ionospheric energy input is approximately equal to the change in magnetic energy in the subsequent dipolarization. However, the good correlation between the two quantities suggests a causal relationship. The approximate equality between the two energy values allows for the 20% change in Sym-H during dipolarization caused by disruption of the tail current estimated by Ohtani et al. (2001). Similarly, this result does not conflict with the conjecture by Siscoe and Petschek (1997) that Joule heating associated with the diversion of the tail current through the ionosphere also contributes to Sym-H recovery at these times; Joule heating continues through the growth and expansion phases of the substorm. Our results show the approximate equivalency between the energy stored in the magnetotail during the substorm growth phase and the Joule

heat dissipation occurring at the same time. Adopting the lumped circuit analogy used by Siscoe and Petschek (1997), the solar wind energy input to the magnetosphere during the substorm growth phase is split approximately equally between magnetic energy storage (inductance) in the tail and Joule heating (resistance) in the ionosphere.

Inherent in the model used here to calculate Joule heating is the increase in conductance with the strength of the field-aligned currents that connect the magnetospheric and ionospheric parts of the circuit. Robinson et al. (2016), (2017), and Zanetti et al. (2018) have previously attributed the impulsive nature of Joule heating events to this increase in ionospheric conductance with field-aligned current density. This causes runaway current conditions, where increasing current enhances the conductance, allowing the current to grow nonlinearly. By this mechanism, electrostatic energy in the magnetosphere is impulsively dissipated through the Joule heating associated with the ionospheric currents. This nonlinear increase is suggested by Figure 2d, which shows the variation of Joule heat with cross polar cap potential. The results shown here suggest that the rapid loss of energy to the ionosphere during the substorm growth phase can interrupt the storage of magnetic energy in the tail. Whether this disruption can actually trigger substorm dipolarization remains to be demonstrated. The 70-min delay may be a result of the time required for field-aligned currents to increase along with the associated ionospheric conductance during the substorm growth phase. Note that Ohtani et al. (2001) and Siscoe and Petschek (1997) focused on the large substorms that occur at the time of maximum Sym-H disturbance during geomagnetic storms. Our results suggest that the same process can occur throughout geomagnetically active periods and with individual substorm-like events occurring on the order of 10 min.

Studies of magnetospheric response to solar wind forcing have demonstrated that the behavior is suggestive of a system that is subject to both external and internal processes (see, for example, Tsurutani et al., 1990). Hnat et al. (2005) and Uritsky et al. (2002) showed that variations of geomagnetic indices shorter than 2–4 h are not directly driven by the solar wind. By analyzing time series of AE indices, Pulkkinen et al. (2006) demonstrated that fluctuations in the response to solar wind forcing are of internal magnetospheric origin, even though they are powered by external forcing. These stochastic fluctuations are impulsive in nature, as suggested by Sergeev et al. (1996), who referred to them as impulsive dissipation events. Although the existence of these stochastic processes and impulsive events has been demonstrated, their origin has not been identified. Our results suggest that the rapid increase of Joule heating through field-aligned currents and time varying conductances is a likely explanation for such an internal mechanism.

6. Conclusions

This study of 27 geomagnetically active days shows how energy input to the ionosphere from particle precipitation and Joule heating varies with increasing activity levels. Joule heating exceeds energy input from particle precipitation by about a factor of two during active periods and is impulsive in nature. These impulsive Joule heating events correlate well with recoveries in the Sym-H index, with the maximum correlation when the Joule heating is compared to Sym-H recoveries 70 min later. Because prior studies have shown that substorm-related dipolarizations of magnetic fields are associated with transient recoveries in Sym-H, the observed time delay suggests that enhancements in Joule heating occur during the substorm growth phase prior to diversion of tail currents that produce magnetic field dipolarization. The good correlation between the two time-shifted quantities indicates that the amount of magnetic energy released during dipolarization events is approximately equal to the energy lost to the ionosphere over the same time interval during the substorm growth period. We speculate that the increasing field-aligned currents and ionospheric conductances during substorm growth causes a nonlinear increase in energy dissipation by Joule heating, eventually disrupting the magnetic energy storage process. The determination of ionospheric energy input from particle precipitation and Joule heating derived from AMPERE maps of field-aligned currents offers the means for a more detailed study of the temporal and spatial characteristics of these processes.

Data Availability Statement

AMPERE data used in this study are publically available through the AMPERE web site: http://ampere.jhuapl.edu. AE and Sym-H data were obtained from the Data Analysis Center for Geomagnetism and Space Magnetism, Graduate School of Science, Kyoto University through its web site at http://wdc.kugi.kyoto-u.ac.jp/index.html.

Acknowledgments
This work was supported at Goddard Space Flight Center by NASA Cooperative Agreement NNG11PL10A, the Community Coordinated Modeling Center, and the TIMED/GUVI Project (NASA grant NNX14AK74G).

References

Anderson, B. J., North, H., Waters, C. L., Green, D. L., Merkin, V. G., Barnes, R. J., et al. (2014). Development of large-scale Birkeland currents determined from the Active Magnetosphere and Planetary Electrodynamics Response Experiment. *Geophysical Research Letters*, *41*. https://doi.org/10.1002/2014GL059941

Anderson, B. J., Takahashi, K., & Toth, B. A. (2000). Sensing global Birkeland currents with Iridium engineering magnetometer data. *Geophysical Research Letters*, *27*(24), 4045–4048. https://doi.org/10.1029/2000GL000094

Cousins, E. D. P., Matsuo, T., & Richmond, A. D. (2015). Mapping high-latitude ionospheric electrodynamics with SuperDARN and AMPERE. *Journal of Geophysical Research – A: Space Physics*, *120*, 5854–5870. https://doi.org/10.1002/2014JA020463

Crowley, G., & Hackert, C. L. (2001). Quantification of high latitude electric field variability. *Geophysical Research Letters*, *28*(14), 2783–2786. https://doi.org/10.1029/2000GL012624

Dessler, A. J., & Parker, E. N. (1959). Hydromagnetic theory of geomagnetic storms. *Journal of Geophysical Research*, *64*, 2239–2252. https://doi.org/10.1029/JZ064i012p02239

Gjerloev, J. W. (2009). A global ground-based magnetometer initiative. *Eos, Transactions American Geophysical Union*, *90*, 230–231. https://doi.org/10.1029/2009EO270002

Gjerloev, J. W. (2012). The SuperMAG data processing technique. *Journal of Geophysical Research*, *117*, A09213. https://doi.org/10.1029/2012JA017683

Hnat, B., Chapman, S. C., & Rowlands, G. (2005). Scaling and a Fokker-Planck model for fluctuations in geomagnetic indices and comparison with solar wind ε as seen by Wind and ACE. *Journal of Geophysical Research*, *110*, A08206. https://doi.org/10.1029/2004JA010824

Iyemori, T., & Rao, D. R. K. (1996). Decay of the Dst field of geomagnetic disturbance after substorm onset and its implication to storm-substorm relation. *Annals of Geophysics*, *1*, 608–618.

Janhunen, P., Palmroth, M., Laitinen, T., Honkonen, I., Juusola, L., Facsko, G., et al. (2012). The GUMICS-4 global MHD magnetosphere-ionosphere coupling simulation. *Journal of Atmospheric and Solar-Terrestrial Physics*, *80*, 48–59.

Liemohn, M. W. (2003). Yet another caveat to using the Dessler-Parker-Sckopke relation. *Journal of Geophysical Research*, *108*, 1251. https://doi.org/10.1029/2003JA009839

Lu, G., & Richmond, A. D. (1996). Specification and forecast of ionospheric conditions with AMIE. In *The Evaluation of Space Weather Forecasts* (pp. 35–38). Boulder, CO: Proceedings of a Workshop June 19-21.

Newell, P. T., Liou, K., Zhang, Y., Paxton, L. J., & Mitchell, E. J. (2014). OVATION Prime-2013: Extension of auroral precipitation model to higher disturbance levels. *Space Weather*, *12*, 368–379. https://doi.org/10.1002/2014SW001056

Newell, P. T., Sotirelis, T., & Wing, S. (2009). Diffuse, monoenergetic, and broadband aurora: The global precipitation budget. *Journal of Geophysical Research*, *114*, A09207. https://doi.org/10.1029/2009JA014326

Ohtani, S., Nosé, M., Rostoker, G., Singer, H., Lui, A. T. Y., & Nakamura, M. (2001). Storm-substorm relationship: Contribution of the tail current to Dst. *Journal of Geophysical Research*, *106*(A10), 21199–21209. https://doi.org/10.1029/2000JA000400

Pulkkinen, A., Klimas, A., Vassiliadis, D., & Uritsky, V. (2006). Role of stochastic fluctuations in the magnetosphere-ionosphere system: A stochastic model for the AE index variations. *Journal of Geophysical Research*, *111*, A10218. https://doi.org/10.1029/2006JA011661

Qian, L., Burns, A. G., Emery, B. A., Foster, B., Lu, G., Maute, A., et al. (2014). The NCAR TIE-GCM: A community model of the coupled thermosphere/ionosphere system. In J. Huba, R. Schunk, & G. Khazanov (Eds.), *Modeling the Ionosphere-Thermosphere System* (pp. 73–84). Washington, DC: John Wiley & Sons. https://doi.org/10.1002/9781118704417.ch7

Richmond, A. D. (1992). Assimilative mapping of ionospheric electrodynamics. *Advances in Space Research*, *12*(6), 26681–26696. https://doi.org/10.1029/96JA01285

Ridley, A. J., Deng, Y., & Toth, G. (2006). The global ionosphere-thermosphere model. *Journal of Atmospheric and Solar-Terrestrial Physics*, *68*, 839–864. https://doi.org/10.1016/j.jastp.2006.01.008

Robinson, R. M., Kaeppler, S. R., Zanetti, L., Anderson, B. J., Vines, S. K., Korth, H., et al. (2020). Statistical relations between auroral electrical conductances and field-aligned currents at high latitudes. *Journal of Geophysical Research*, *125*, e2020JA028008. https://doi.org/10.1029/2020JA028008

Robinson, R. M., Zanetti, L. J., Anderson, B. J., & Korth, H. (2017). High latitude energy deposition during geomagnetic storms determined from AMPERE observations. In *Annual Meeting, 14th Conference on Space Weather*. American Meteorological Society.

Robinson, R. M., Zanetti, L. J., Anderson, B. J., Korth, H., Samara, M., Michell, R., et al. (2016). *High latitude precipitating energy flux and Joule heating during geomagnetic storms determined from AMPERE field-aligned currents*. American Geophysical Union, Fall General Assembly Abstract id: SM53A-06.

Robinson, R. M., Zanetti, L., Anderson, B. J., Vines, S. K., and Gjerloev, J. (2020). *Determination of auroral energy flux and electrodynamic parameters from AMPERE field-aligned current measurements*. Space Weather.

Robinson, R. M., Zhang, Y., Anderson, B. J., Zanetti, L. J., Korth, H., & Fitzmaurice, A. (2018). Statistical relations between field-aligned currents and precipitating electron energy flux. *Geophysical Research Letters*, *45*, 8738–8745. https://doi.org/10.1029/2018GL078718

Roble, R. G., & Emery, B. A. (1983). On the global mean temperature of the thermosphere. *Planetary and Space Science*, *31*(6), 597–614. https://doi.org/10.1016/0032-0633(83)90002-8

Roble, R. G., & Ridley, E. C. (1987). An auroral model for the NCAR thermospheric general circulation model (TGCM). *Annales Geophysicae Series A: Upper Atmosphere And Space Sciences*, *5*, 369–382.

Sergeev, V. A., Pulkkinen, T. I., & Pellinen, R. J. (1996). Coupled-mode scenario for the magnetospheric dynamics. *Journal of Geophysical Research*, *101*(A6), 13047–13066. https://doi.org/10.1029/95JA03192

Siscoe, G. L., & Petschek, H. E. (1997). On storm weakening during substorm expansion phase. *Annals of Geophysics*, *15*, 211–216.

Tsurutani, B. T., Sugiura, M., Iyemori, T., Goldstein, B. E., Gonzalez, W. D., Akasofu, S. I., et al. (1990). The nonlinear response of AE to the IMF Bs driver: A spectral break at 5 hours. *Geophysical Research Letters*, *17*, 279–282. https://doi.org/10.1029/GL017i003p00279

Uritsky, V., Klimas, A., Vassiliadis, D., Chua, D., & Parks, G. (2002). Scale-free statistics of spatiotemporal auroral emissions as depicted by POLAR UVI images: Dynamic magnetosphere is an avalanching system. *Journal of Geophysical Research*, *107*(A12), 1426. https://doi.org/10.1029/2001JA000281

Weimer, D. R. (1995). Models of high-latitude electric potentials derived with a least error fit of spherical harmonic coefficients. *Journal of Geophysical Research*, *100*, 19595–19607. https://doi.org/10.1029/95JA01755

Weimer, D. R. (2005). Improved ionospheric electrodynamic models and application to calculating Joule heating rates. *Journal of Geophysical Research*, *110*, A05306. https://doi.org/10.1029/2004JA010884

Weimer, D. R., N. C. Maynard, W. J. Burke, & C. Liebrecht (1990). Polar cap potentials and the auroral electrojet indices. *Planetary and Space Science*, *38*(9), 1207–1222. https://doi.org/10.1016/0032-0633(90)90028-O

Zanetti, L., R. Robinson, B. Anderson, & H. Korth (2018). Impulsive energy transfer from the magnetosphere to the ionosphere during geomagnetic storms. *Sun and Geosphere*, *13*, 169–172. https://doi.org/10.31401/SunGeo.2018.02.08